Enhanced Beluga Whale Optimisation for joint inversion of seismic refraction and surface-wave dispersion: towards advanced near-surface characterisation

Fengjun WU[1,*], Xinai XU[1], Kerong HE[2], Gang LI[1], Zhenlin LEI[3]

[1] School of Mathematics and Information Science, Nanchang Normal University, Nanchang 330032, China;
e-mails: wfj@ncnu.edu.cn, jxxxa@ncnu.edu.cn, 562672612@qq.com

[2] School of Physics and Electronic Information, Nanchang Normal University, Nanchang 330032, China;
e-mail: hekerong_ncnu@163.com

[3] Research Office, Nanchang Normal University, Nanchang 330032, China;
e-mail: leizhenlin0911@163.com

Abstract: Seismic methods constitute indispensable tools for characterising subsurface structures in near-surface geophysical investigations. To address the inherent challenges associated with the joint inversion of Rayleigh wave dispersion curves and seismic refraction data, this study introduces an Enhanced Beluga Whale Optimisation (EBWO) algorithm incorporating two principal advancements. A hybrid initialisation scheme combining Tent chaotic mapping and reverse learning strategies is adopted to substantially enrich population diversity, thereby overcoming the limitations of purely random initialisation employed in the original Beluga Whale Optimisation (BWO). The performance of EBWO is systematically evaluated through a two-stage validation framework. First, benchmark tests on four complex multimodal functions demonstrate that EBWO achieves superior convergence accuracy and enhanced solution stability relative to the standard BWO. Subsequently, synthetic joint inversion experiments under both noise-free and noise-contaminated conditions further verify its robustness and reliability, with EBWO consistently outperforming both BWO and Particle Swarm Optimisation (PSO). The applicability of the proposed approach is further demonstrated using field datasets from Türkiye, where EBWO yields lower data misfits, improved agreement with independent geophysical interpretations and available geological constraints, and greater inversion stability. By integrating surface wave dispersion and refraction datasets within a unified inversion framework, EBWO effectively exploits their complementary sensitivities, thereby alleviating the non-uniqueness inherent in single-method inversions. Overall, the results

*corresponding author, e-mail: wfj@ncnu.edu.cn

doi: 10.31577/congeo.2026.56.2.1

highlight the efficacy and robustness of EBWO for near-surface characterisation and underscore its considerable potential for broader applications in multi-parameter geophysical inversion.

Key words: seismic refraction, Rayleigh wave dispersion, joint inversion, near-surface geophysics

1. Introduction

Seismic methods have become increasingly indispensable for characterising subsurface conditions in near-surface geophysical investigations. Among these, active-source surface-wave analysis plays a pivotal role in the development of geological and geotechnical models, particularly for deriving shear-wave velocity (*Vs*) profiles (*Park et al., 1999; Cao et al., 2025; Pan et al., 2025; Ning et al., 2025, 2026*). In contrast to conventional seismic techniques, such as refraction and reflection methods—which do not directly or efficiently resolve *Vs*—surface-wave analysis offers a more robust and practically viable alternative. A wide range of inversion strategies for active-source surface-wave dispersion has been developed, with many relying on local (deterministic) optimisation techniques. However, dispersion inversion is intrinsically high-dimensional and strongly nonlinear (*Ai et al., 2025a,b; 2026*), rendering such approaches highly sensitive to the choice of the initial model. Gradient-based methods, in particular, require well-constrained starting models to ensure convergence toward physically meaningful solutions; otherwise, they are prone to entrapment in local minima. In recent years, machine learning–based inversion techniques have emerged as promising alternatives. For instance, *Yang et al. (2022)* demonstrated that training on a carefully curated subset of 500 samples from an initial pool of 5000 yielded more accurate and stable *Vs* models than training on the entire dataset. Similarly, *Yang et al. (2023)* proposed a two-stage broad learning framework that effectively reduces the search space and enhances optimisation efficiency while requiring only a limited number of training samples.

Seismic refraction inversion has likewise been extensively investigated using both deterministic and global optimisation approaches. Deterministic techniques include singular value decomposition and the simultaneous iterative reconstruction technique (*Meyer, 2023; Lo and Inderwiesen, 1994*), whereas global optimisation methods—such as Genetic Algorithms (*Michalewicz, 1996*) and the Jellyfish Search Algorithm (*Poormirzaee, 2022*)—have also been widely adopted. Nevertheless, a persistent limitation of refraction methods is the so-called "hidden layer" problem, typically associated with thin low-velocity layers or insufficient receiver spacing. This issue can lead to misinterpretation and the generation of unrealistic subsurface velocity models (*Soske, 1959*).

To mitigate these limitations, joint inversion techniques have attracted considerable attention in recent years. By exploiting the complementary sensitivities of different geophysical datasets, joint inversion enhances model constraints and reduces the non-uniqueness inherent in single-method approaches. Numerous studies have demonstrated the effectiveness of such strategies. For example, *Ivanov et al. (2006)* incorporated *Vs* information derived from surface-wave analysis as constraints in refraction inversion, yielding more geologically consistent models than conventional tomography. Other studies have integrated surface-wave and body-wave datasets to improve near-surface resolution. A one-dimensional joint inversion of Rayleigh-wave dispersion and P-wave travel times was presented in *Piatti et al. (2013)*, while *Poormirzaee (2018)* implemented a multi-objective Particle Swarm Optimisation (PSO) framework for the simultaneous inversion of refraction and surface-wave data. More recently, *Wang et al. (2023)* combined first-arrival travel-time tomography (FATT) with multichannel analysis of surface waves (MASW) to further enhance subsurface imaging. Joint inversion can be implemented using either local or global optimisation strategies; however, global optimisers are generally preferred due to their ability to explore complex model spaces and approximate global optima. A wide variety of global optimisation algorithms have been applied to geophysical inversion, including the Genetic Algorithm (*Michalewicz, 1996*), PSO (*Song et al., 2012*), Shuffling Frog Hopping Algorithm (*Sun et al., 2017*), Adaptive Chaotic Genetic PSO (*Yang et al., 2019*), Grasshopper Algorithm (*Yu et al., 2019*), Adaptive Dragonfly Optimisation (*Gao et al., 2021*), Modified Barnacles Mating Optimiser (*Ai et al., 2024a*), Jellyfish Search Algorithm (*Poormirzaee, 2022*), Lightning Attachment Optimiser (*Fu et al., 2023a*), Sine Cosine Algorithm (SCA) (*Fu et al., 2023b*), Modified Success-History-based Adaptive Differential Evolution (*Ekinci et al., 2023, 2025a*), Improved Butterfly Optimisation Algorithm (*Peng et al., 2024*), Improved Wild Horse

Optimisation (*Tang and Wu, 2024*), Improved Backtracking Search Optimisation Algorithm (*Balkaya et al., 2024*), and Hunger Games Search (*Su et al., 2024; Ai et al., 2024b, 2025a; Ekinci et al., 2025b*). Despite these advances, global optimisation methods remain sensitive to algorithm-specific parameters and predefined model bounds, and their performance can vary significantly depending on the problem context (*Yang et al., 2024*). In particular, some algorithms suffer from slow convergence rates, high computational demands, or limited solution accuracy.

A central challenge in global optimisation lies in maintaining an appropriate balance between exploration and exploitation. Exploration facilitates the broad sampling of the model space and promotes diversity, whereas exploitation intensifies the search around promising candidate solutions. Excessive exploration may hinder convergence efficiency, while excessive exploitation increases the risk of premature convergence to local optima. Achieving an effective balance between these competing processes is therefore critical for robust and efficient inversion.

The Beluga Whale Optimisation (BWO) algorithm, introduced by *Zhong et al. (2022)*, is a swarm intelligence technique inspired by the foraging and migratory behaviours of beluga whales in Arctic environments. By mimicking mechanisms, such as spiral predation and group foraging, the BWO is capable of balancing global exploration and local exploitation, making it well suited for solving high-dimensional, multimodal optimisation problems. However, its performance may be constrained by insufficient population diversity during the evolutionary process.

To address these limitations, this study develops an Enhanced Beluga Whale Optimisation (EBWO) algorithm that integrates Tent chaotic mapping and opposition-based learning. These strategies enhance population diversity during initialisation, improve global exploration, and accelerate convergence toward the global optimum. The performance of EBWO is first evaluated using four standard benchmark functions and compared with the original BWO and Particle Swarm Optimisation (PSO). It is then applied to synthetic joint inversion experiments of Rayleigh-wave dispersion and seismic refraction data under both noise-free and noisy conditions, followed by validation using field datasets from Türkiye with complex geological settings. Finally, the limitations of the approach and potential directions for future research are discussed.

2. BWO and EBWO

The Beluga Whale Optimisation (BWO) algorithm is a nature-inspired metaheuristic that emulates the swimming, foraging, and sinking behaviours of beluga whales in marine environments. The algorithm is structured around three principal evolutionary phases—exploration, exploitation, and whale fall—which correspond to the whales' collective movement, cooperative predation, and post-mortem sinking processes, respectively. *Wu et al. (2025)* used it for dispersion inversion. The mathematical formulation of the algorithm is outlined as follows.

2.1. Initialisation

Within the BWO framework, each beluga whale represents a candidate solution (search agent) in the model space. The initial population is generated by randomly sampling of the search domain:

$$X_j^i = Lb_j + (Ub_j - Lb_j) \times \mathrm{rand}\,. \tag{1}$$

To regulate the transition between global exploration and local exploitation, a balance factor B_f is introduced:

$$B_f = B_0 \cdot \left(1 - \frac{t}{T_{\max}}\right)\,, \tag{2}$$

where B_0 is a uniformly distributed random number between (0,1), t denotes the current iteration index, and $T_{\max}$ is the maximum number of iterations. When $B_f > 0.5$, the population operates in the exploration phase; conversely, when $B_f < 0.5$, the algorithm transitions to the exploitation phase.

2.2. Exploration phase

The exploration phase of the BWO algorithm simulates the social behaviour of beluga whales swimming in pairs, moving randomly in a synchronised or mirrored manner. The position update is as follows:

$$\begin{cases} x_{i,j}^{t+1} = x_{i,p}^t + (x_{r,p}^t - x_{i,p}^t)(1 + r_1) \cdot \sin(2\pi r_2), & j = 2, 4, 6, ... \\ x_{i,j}^{t+1} = x_{i,p}^t + (x_{r,p}^t - x_{i,p}^t)(1 + r_1) \cdot \cos(2\pi r_2), & j = 1, 3, 5, ... \end{cases} \tag{3}$$

where $x_{i,j}^{t+1}$ represents the position of the individual in the next iteration; p

is a random integer within the range [1, D], D being the problem dimension; $x_{i,p}^t$ represents the value of the i-th individual in the p-th dimension, $x_{r,p}^t$ represents the value of a random individual r in a random dimension p during the current iteration, and r_1 and r_2 are random numbers.

2.3. Exploitation phase

The exploitation phase emulates cooperative hunting behaviour, wherein individuals converge towards promising regions of the search space through information sharing. To further enhance convergence efficiency and avoid local optima, a Lévy flight mechanism is incorporated. The update scheme is expressed as:

$$x_i^{t+1} = r_3 \cdot x_{\text{best}}^t - r_4 \cdot x_i^t + C_1 \cdot L_F \cdot (X_r^t - x_i^t)\,, \tag{4}$$

$$C_1 = 2 \cdot r_4 \cdot \left(1 - \frac{t}{T_{\max}}\right), \tag{5}$$

where r_3 and r_4 are random numbers; x_i^t and x_{best}^t represent the positions of a random individual and the best individual, respectively; C_1 is a step size control parameter measuring the intensity of the Lévy flight. L_F represents the Lévy flight function:

$$L_F = 0.05 \times \frac{\mu \cdot \sigma}{|\nu|^{\frac{1}{\beta}}}\,, \tag{6}$$

$$\sigma = \left(\frac{\Gamma(1+\beta) \times \sin\left(\pi \cdot \frac{\beta}{2}\right)}{\Gamma\left(\frac{1+\beta}{2}\right) \times \beta \times 2^{\frac{\beta-1}{2}}} \right)^{\frac{1}{\beta}}, \quad \Gamma(x) = (x-1)!\,, \tag{7}$$

where $u, v \sim N(0,1)$ are random numbers following a normal distribution with mean 0 and variance 1, and β is a constant set to 1.5.

2.4. Whale fall phase

The whale fall phase represents the sinking of beluga whales to the ocean floor, introducing additional stochastic perturbations that help maintain population diversity and prevent premature convergence. This phase is activated when $B_f \leq W_f$, where W_f is the whale fall probability. The position update is defined as:

$$x_i^{t+1} = r_5 \cdot x_i^t - r_6 \cdot x_r^t + r_7 \cdot x_{\text{step}}^t \,, \tag{8}$$

$$x_{\text{step}}^t = \mathrm{e}^{\frac{-C_2 \cdot t}{T}} \cdot (Ub - Lb) \,, \tag{9}$$

$$C_2 = 2\, W_f \times N \,, \tag{10}$$

$$W_f = 0.1 - 0.05 \cdot \frac{t}{T_{\max}} \,, \tag{11}$$

where r_5, r_6, and r_7 are random numbers between 0 and 1; Ub and Lb are the upper and lower bounds of the optimisation problem, respectively; x_{step}^t represents the whale fall step size; C_2 represents a step factor; W_f represents the whale fall probability for a beluga individual.

To overcome the limitations associated with insufficient population diversity and slow convergence, two enhancement strategies are incorporated into the original BWO framework.

First, a Tent chaotic mapping scheme is employed for population initialisation, replacing conventional random sampling. Among various chaotic sequences, the Tent map is favoured for its superior ergodicity and uniform distribution characteristics (*Shan et al., 2005*). To mitigate the influence of unstable periodic points, a stochastic perturbation term is introduced (*Zhang et al., 2020*):

$$x_{n+1} = \begin{cases} \frac{1}{p}\left(x_n + \frac{1}{N} \times \text{rand}(0,1)\right), & 0 \le x_n \le p \\ \frac{1}{p}\left(1 - x_n + \frac{1}{N} \times \text{rand}(0,1)\right), & p \le x_n \le 1 \end{cases} \tag{12}$$

where $p = 0.5$, N is taken as the number of chaotic sequence particles, $\text{rand}(0,1)$ is a random number in the interval $[0,1]$, and the random variable $\text{rand}(0,1) \times \frac{1}{N}$ ensures randomness and restricts the random value within a certain range to ensure its regularity. Mapping chaotic sequences to individual solutions:

$$x_{\text{new}} = \min + (\max - \min)\, x_{\text{old}} \,. \tag{13}$$

This strategy significantly enhances the diversity and quality of the initial population, thereby improving the global exploration capability and accelerating convergence. Second, an opposition-based learning (OBL) strategy is incorporated to further refine the initial population:

$$x_{\text{new2}} = \min + \max - x_{\text{old}} \,. \tag{14}$$

By simultaneously considering candidate solutions and their opposites, this approach reduces search bias and improves the likelihood of locating high-quality regions within the search space. The integration of Tent chaotic initialisation and opposition-based learning constitutes the Enhanced Beluga Whale Optimisation (EBWO) algorithm.

3. Benchmark function validation

The performance of EBWO is evaluated using four widely adopted two-dimensional benchmark functions characterised by highly multimodal landscapes and numerous local minima. These functions provide a stringent test of the global optimisation capability. As summarised in Table 1, EBWO

Table 1. Results of applying BWO and EBWO (with the proposed enhancements) to four challenging benchmark functions over 30 independent runs (population size $N = 300$, maximum iterations $T = 100$).

Name	Expression	Search space	Global optimum	BWO	BWO with Tent chaos mapping strategy	BWO with reverse learning strategy	EBWO
Ackley	*AckExp*	[−5, 5]	0	3.24e−07 1.05e−06	13.73e−9 0.1215	7.14e−10 0	8.68e−16 0
Rastrigin	*RasExp*	[−5.12, 5.12]	0	0.0007 0.0097	0.5413 0.2280	0.2779 0	0 0
Eggholder	*EggExp*	[−512, 512]	−959.6407	−833.5436 47.2318	−626.7226 7.6793	−634.7731 5.7892	−958.7331 9.0074
Schwefel	*SchExp*	[−500, 500]	0	58.4832 45.5263	0.8552 0.2673	0.4015 0.4956	0.0028 0.0014

Note: *dim* denotes the dimensionality, with a default value of $dim = 2$. In the last two columns, the blue values represent the mean results of BWO and EBWO over 30 independent runs, while the green values indicate the corresponding standard deviations. The notation "e−16" denotes scientific notation for 10^{-16}. Two-dimensional visualisations of the benchmark functions are available at `http://www.sfu.ca/~ssurjano`.

AckExp: $F_1 = -a\,\exp\left(-b\sqrt{\frac{1}{dim}\sum_{i=1}^{dim} x_i^2}\right) - \exp\left[\frac{1}{dim}\sum_{i=1}^{dim}\cos(cx_i)\right] + a + \exp(1)$,

$a = 20, b = 0.2, c = 2\pi$;

RasExp: $F_2 = 10\,dim + \sum_{i=1}^{dim}\left[x_i^2 - 10\,\cos(2\pi x_i)\right]$;

EggExp: $F_3 = -(x_2 + 47)\sin\sqrt{\left|x_2 + \frac{x_1}{2} + 47\right|} - x_1 \sin\sqrt{|x_1 - (x_2 + 47)|}$;

SchExp: $F_4 = 418.9829\,dim - \sum_{i=1}^{dim} x_i \sin\sqrt{x_i}$.

consistently outperforms the original BWO across all benchmark functions, yielding lower mean objective values and reduced standard deviations over 30 independent runs (population size ($N = 300$), maximum iterations ($T = 100$)). These results demonstrate that the proposed enhancements—namely chaotic initialisation and opposition-based learning—substantially improve both convergence efficiency and solution stability.

4. Synthetic tests with and without noise contamination

We designed a four-layer synthetic model that reflects the typical near-surface conditions encountered in engineering practice (*Yamanaka and Ishida, 1996*) to assess EBWO's performance for simultaneously inverting Rayleigh wave dispersion curves and refraction data. The true model parameters and their search ranges are listed in Table 2. Regarding this joint inversion framework, the coupling parameters of the dispersion and refraction data are Vp and h. The joint inversion objective function, *Obj*, is thus defined as follows:

$$Obj(h, Vs, Vp) = w_1 \sqrt{\sum_{i=1}^{M_1} \sum_{r=1}^{R} \frac{\left[V_{obs}^{r}(f_i) - V_{cal}^{r}(f_i, h, Vs, Vp)\right]^2}{V_{obs}^{r}(f_i)^2}} + \\ + w_2 \sqrt{\sum_{i=1}^{M_2} \frac{\left[V_{obs}^{f}(x_i) - V_{cal}^{f}(x_i, h, Vp)\right]^2}{V_{obs}^{f}(x_i)^2}}, \tag{15}$$

where:

- V_{obs}^{r} and V_{cal}^{r} are the observed and calculated Rayleigh wave phase velocities.
- M_1 represents the total number of frequency samples.
- Here, R is the order of the dispersion curve (only the fundamental mode, $R = 1$, is considered herein).
- V_{obs}^{f} and V_{cal}^{f} are the observed and calculated first-arrival times.
- M_2 is the number of refraction picks.
- w_1 and w_2 are the weighting factors, $w_1 = w_2$ in this study, assuming equal contribution achieved by the two datasets as recommended by *Ai et al. (2025b)*.

The density parameter of the forward modelling of dispersion curves is fixed as the common practice given within (*Xia et al., 1999, 2003*). The dispersion curve is forward-modelled with the stiffness-matrix method of *Fan et al. (2002)*, while the refraction travel times are computed using the layered-earth ray-tracing formulation of *Poormirzaee (2022)*.

Table 2. Model parameters of the synthetic model and the determined large model space.

Layers	Model parameters				Model space		
	Vs (m/s)	Vp (m/s)	ρ (g/cm^3)	h (m)	Vs (m/s)	h (m)	Vp (m/s)
1	220	350	1.8	2	$100 \sim 350$	$1 \sim 5$	$100 \sim 600$
2	420	700	1.7	10	$200 \sim 500$	$5 \sim 20$	$300 \sim 1000$
3	260	450	1.8	5	$100 \sim 500$	$2 \sim 8$	$200 \sim 1000$
Half-space	710	1200	1.9	∞	$300 \sim 1100$	∞	$600 \sim 2000$

Note: the density parameter is fixed using empirical relationships (*Xia et al., 1999, 2003*).

4.1. Synthetic test without noise contamination

This section presents the application of BWO, EBWO, and Particle Swarm Optimisation (PSO) to the joint inversion of seismic refraction travel-time and Rayleigh wave dispersion curve (restricted to the fundamental mode, as noted previously) under noise-free conditions. For the PSO implementation, the algorithmic parameters were set to $w = 0.729$, $c_1 = 2.041$, $c_2 = 0.948$, where w denotes the inertia weight and c_1 and c_2 represent the cognitive and social learning coefficients, respectively, following the parameterisation proposed in *Ai et al. (2025a)*.

The Rayleigh wave dispersion dataset spans a frequency range of 5–80 Hz with a sampling interval of 1 Hz, while synthetic seismic refraction travel times were generated using a spatial sampling interval of 2 m over source–receiver offsets ranging from 5 to 50 m. Each algorithm was executed with a fixed population size of 300 and a maximum of 100 iterations. To account for the stochastic variability inherent in metaheuristic optimisation, each inversion experiment was independently repeated 30 times. The reported inversion results correspond to the ensemble mean of these runs, with the associated standard deviation employed as a quantitative measure of solution stability.

To explicitly evaluate the benefits of data integration, each algorithm was also applied to individual inversion scenarios using either the fundamental-mode Rayleigh wave dispersion data or the refraction dataset alone. All inversion parameters were held constant across joint and individual cases to ensure methodological consistency and comparability. The corresponding data-fitting results obtained by BWO, EBWO, and PSO are illustrated in Fig. 1. All three algorithms achieve satisfactory fits to the observed dispersion curves and travel-time data; however, notable differences emerge in the reconstructed subsurface velocity models.

As shown in Fig. 2, EBWO consistently outperforms the other algorithms in recovering both shear-wave velocity Vs and P-wave velocity Vp structures. The velocity profiles obtained using EBWO (blue/yellow solid lines in Figs. 2a–2b) exhibit the closest agreement with the reference models (black

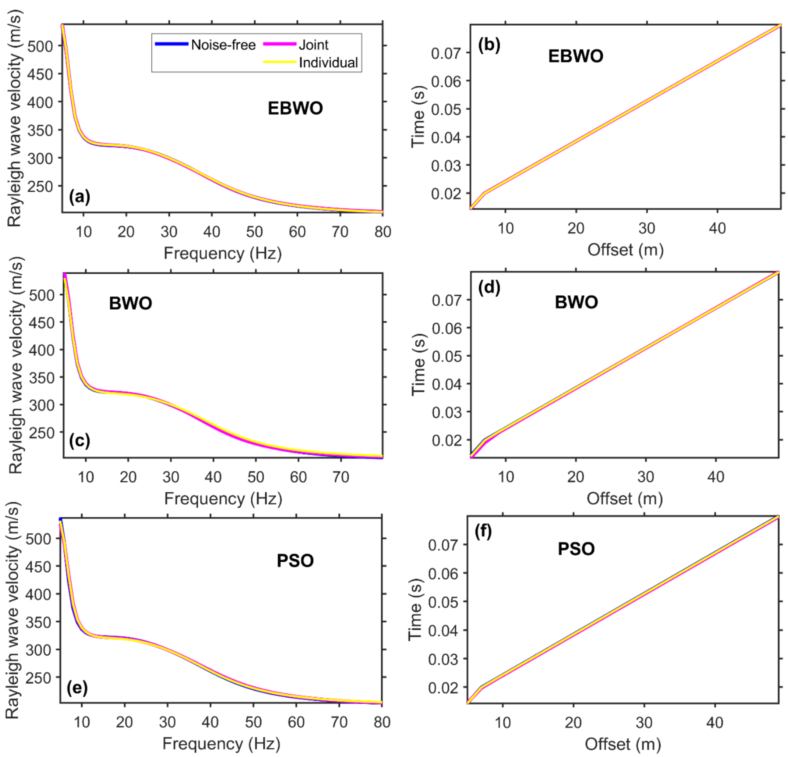

Fig. 1. Joint and independent inversion results for noise-free fundamental mode Rayleigh wave dispersion and refraction data using BWO, EBWO, and PSO. Blue curves denote the noise-free observed data; pink curves represent joint inversion results; yellow curves correspond to independent inversion results. Subplots (a)–(f) display the dispersion and refraction data fits obtained using BWO, EBWO, and PSO, respectively.

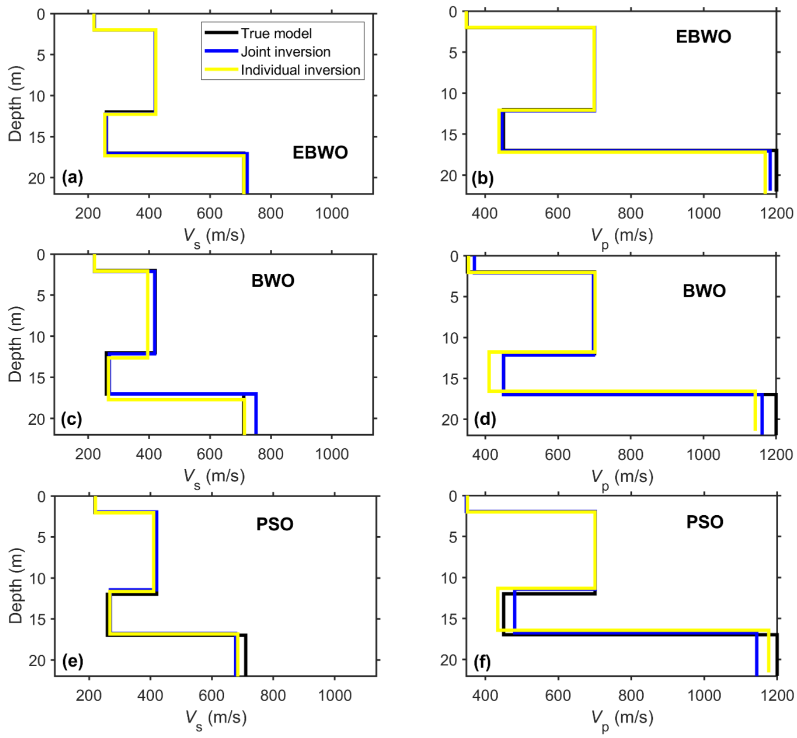

Fig. 2. Joint and independent inversion results of noise-free synthetic data using BWO, EBWO, and PSO. Black: true model; blue: joint inversion; yellow: independent inversion. Subplots (a)–(f) show inverted shear wave velocity and P-wave profiles for each algorithm.

solid lines) under both joint and individual inversion schemes. In contrast, the models derived from BWO and PSO display more pronounced deviations from the true subsurface structure.

Furthermore, Figure 2 demonstrates that the performance of EBWO is significantly enhanced under joint inversion relative to individual inversion, underscoring the advantages of integrating complementary geophysical datasets. For BWO and PSO, the improvements associated with joint inversion are comparatively modest, indicating that although acceptable data fits are achieved, the recovered model parameters remain subject to substantial uncertainty. These discrepancies reflect the intrinsic non-uniqueness of geophysical inversion and highlight the superior resolving capability of EBWO in navigating complex model spaces.

Figure 3 illustrates the convergence behaviour of the three algorithms during joint inversion, with a logarithmic scale applied to the horizontal axis to better resolve the early-stage convergence dynamics. While all methods exhibit comparable initial convergence trends, EBWO consistently attains the lowest final misfit, in agreement with the improved model accuracy observed in Fig. 2. In contrast, BWO and PSO converge to higher residual misfits, suggesting a greater susceptibility to premature convergence and entrapment in local minima.

Table 3 summarises the statistical inversion performance across 30 independent runs, including the mean parameter estimates, standard deviations, and relative error metrics for each model parameter. EBWO yields the lowest maximum relative errors and the smallest standard deviations, thereby demonstrating superior accuracy, robustness, and repeatability compared with BWO and PSO.

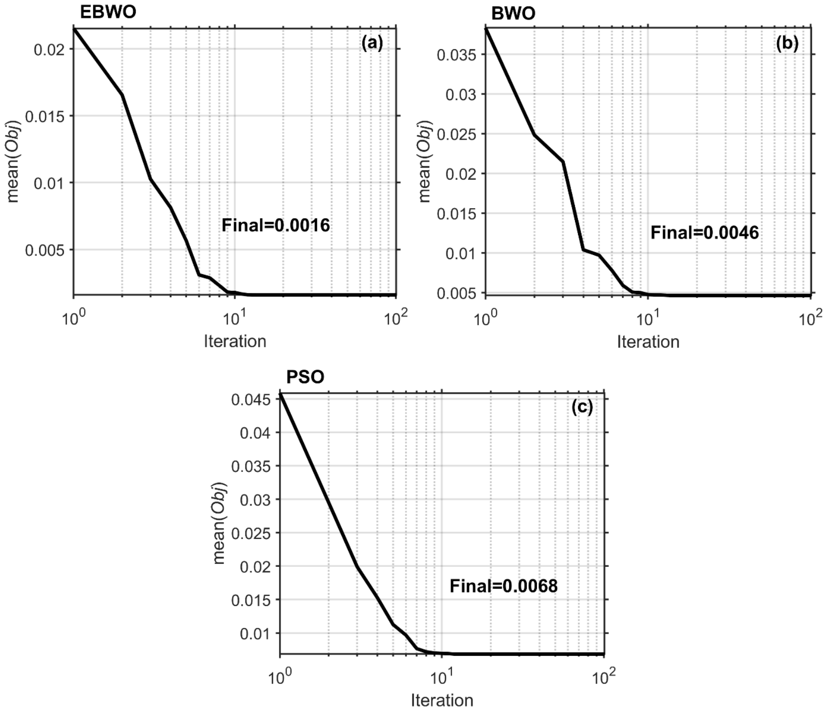

Fig. 3. Iteration process of joint inversion of noise-free Rayleigh wave dispersion curves and refraction data using EBWO (a), BWO (b), and PSO (c).

In summary, the results confirm that EBWO provides highly accurate and stable solutions for the joint inversion of noise-free Rayleigh wave dispersion and seismic refraction data. Relative to BWO and PSO, EBWO exhibits an enhanced global search capability and improved resistance to local minima. Moreover, joint inversion using EBWO consistently outperforms individual inversion approaches, reinforcing the value of integrating complementary geophysical datasets to obtain more reliable and well-constrained subsurface models.

4.2. Synthetic tests with noise

To simulate a more realistic acquisition scenario in which observational data are contaminated by noise, a 10% noise level was introduced into both the theoretical Rayleigh wave dispersion curves and seismic refraction travel-time data according to Eq. (16) (*Ai et al., 2025a*):

$$\begin{aligned} \mathit{Noisy\ data} = \mathit{data} + \mathit{NR} \times \mathrm{mean}[\mathit{data}] \times [\mathrm{rand}_1(\sim) - \mathrm{rand}_2(\sim)], \\ \mathit{NR} = 10\%\,. \end{aligned} \tag{16}$$

Here, mean[ ] denotes the average value of the input dataset, while $\mathrm{rand}_1(\,)$ and $\mathrm{rand}_2(\,)$ generate random arrays of identical dimensions to the input, with values uniformly distributed in the interval $([0, 1])$.

Under these noise-contaminated conditions, BWO, EBWO, and PSO were applied to both joint and individual inversion schemes using the same parameter settings as those adopted in the noise-free experiments. The corresponding inversion results are presented in Fig. 4.

As illustrated in Figure 4, despite the introduction of noise into both dispersion and refraction datasets, all three optimisation algorithms remain capable of producing satisfactory fits to the theoretical (noise-free) responses under both joint and individual inversion frameworks. However, more pronounced discrepancies emerge in the reconstructed subsurface velocity models. As shown in Fig. 5, the recovered shear-wave and P-wave velocity structures deviate noticeably from the synthetic reference model, particularly for BWO and PSO, which exhibit reduced fidelity in capturing the true subsurface configuration. These deviations can be primarily attributed to the propagation of noise-induced perturbations within the inversion process.

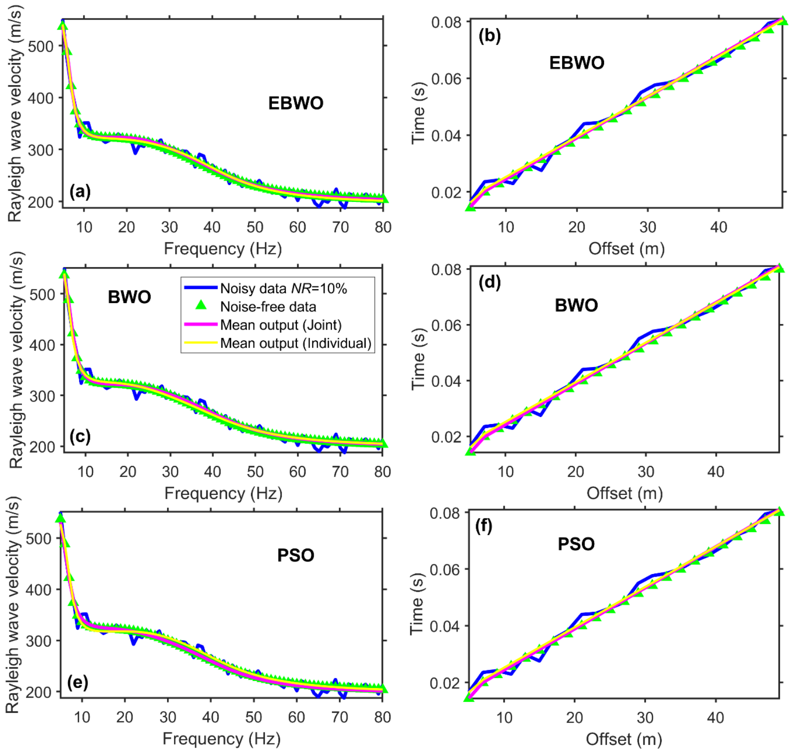

Fig. 4. Joint and independent inversion results for noise-contaminated Rayleigh wave dispersion and refraction data using BWO, EBWO, and PSO. Blue curves denote the noisy data; pink curves represent joint inversion results; yellow curves correspond to independent inversion results; green triangles indicate the noise-free reference data. Further details are provided in the main text.

In contrast, the EBWO consistently yields the most accurate inversion results, with the reconstructed velocity profiles showing the closest agreement with the reference model (Fig. 5). Under noisy conditions, discrepancies between the joint inversion results and the true model become more evident than those observed in individual inversions, reflecting the increased sensitivity of coupled inversion frameworks to data uncertainty and noise contamination.

Figure 6 presents a comparison of the convergence behaviour of the BWO, EBWO, and PSO algorithms during the joint inversion of a noisy dataset, with logarithmic scaling applied to the horizontal axis to enhance the visualisation of early-stage convergence. As expected, the final misfit values for

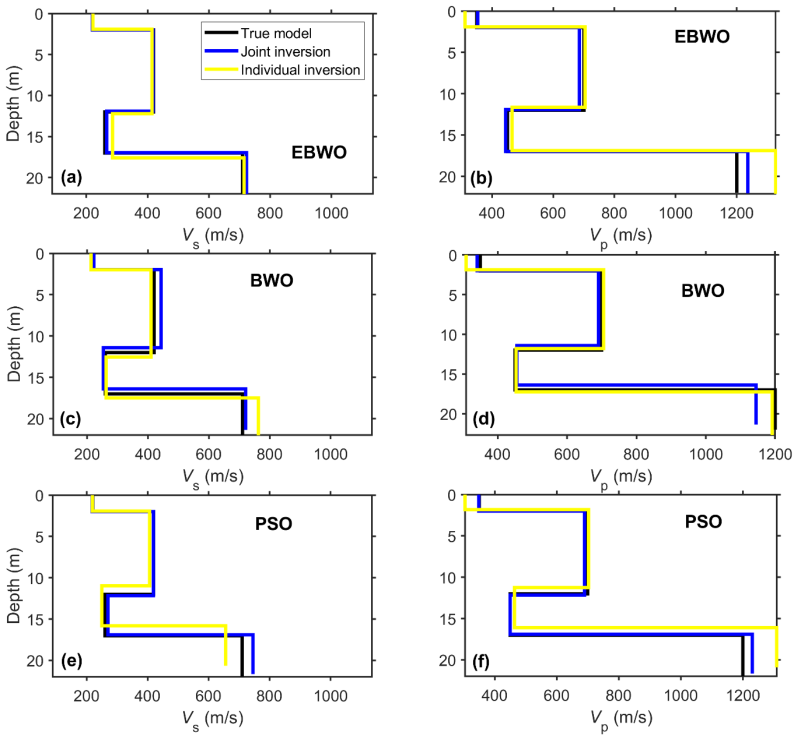

Fig. 5. Joint and independent inversion of noise-contaminated synthetic data using BWO, EBWO, and PSO. Black: true model; blue: joint inversion; yellow: independent inversion. Please refer to the text for more details.

all three algorithms are higher than those obtained in the noise-free case. Nevertheless, the overall convergence trends remain comparable, and the EBWO consistently achieves the lowest residual misfit among the evaluated methods.

The statistical results for joint inversion under noisy conditions, summarised in Table 3, indicate that the presence of noise leads to increased relative errors and greater variability in the estimated model parameters. Despite this degradation, EBWO continues to outperform BWO and PSO in terms of both accuracy and robustness. Even in the presence of substantial data contamination, EBWO reliably produces stable velocity models with low variance and strong consistency with both dispersion and refraction observations.

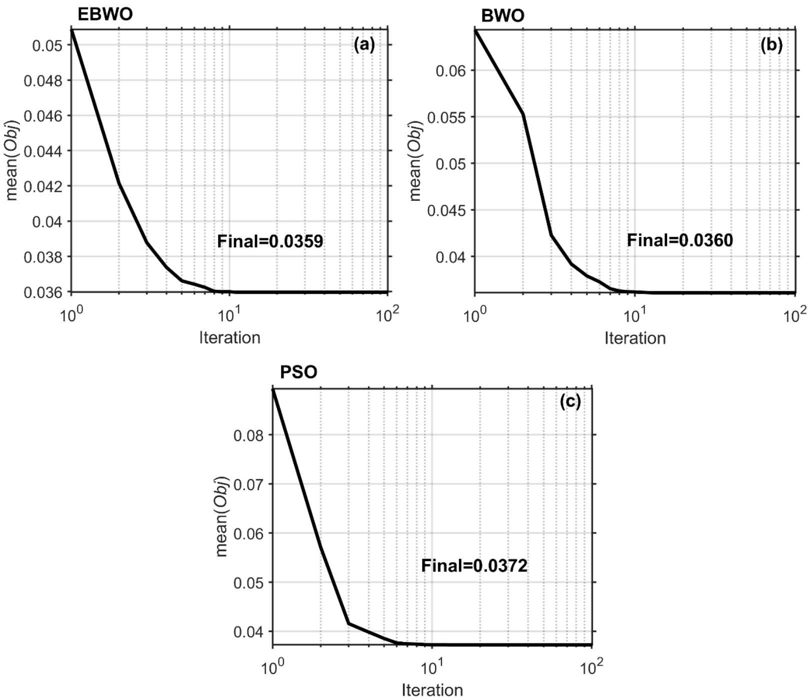

Fig. 6. Iteration process of joint inversion of noise-contaminated Rayleigh wave dispersion curves and refraction data using EBWO (a), BWO (b), and PSO (c).

5. Field data application tests

For the first field case study, *Şenkaya et al. (2020)* acquired multichannel surface-wave and seismic refraction data in the Beşirli area of Trabzon (Ortahisar), Türkiye. The geographic location, topographic setting, and geological framework of the study area are illustrated in Fig. 7 (study area 1). Situated along the Black Sea coastline, the region is potentially influenced by seawater intrusion, which may significantly alter subsurface physical properties.

According to *Şenkaya et al. (2020)*, seismic data were recorded using a 24-channel PASI 16S24-U system equipped with 4.5 Hz vertical geophones. The acquisition parameters comprised a 1 ms sampling interval, a record length of 1024 ms, a geophone spacing of 2 m, and a total spread

Table 3. Comparison of joint inversion performance of EBWO, BWO, and PSO on noise-free and noise-contaminated synthetic models.

	Model parameters	True values	Noise-free			Noise case		
			Mean	Re	STD	Mean	Re	STD
EBWO	v_{s1} (m·s^{-1})	220	220.5	0.0024	0.06	219.8	0.0005	0.18
	v_{s2} (m·s^{-1})	420	420.3	0.0040	2.39	418.1	0.0152	9.03
	v_{s3} (m·s^{-1})	260	258.9	0.0039	0.62	266.1	0.0234	4.12
	v_{s4} (m·s^{-1})	710	721.8	0.0166	11.55	722.5	0.0176	15.25
	h_1 (m)	2	1.9	0.0080	0.02	1.9	0.0092	0.02
	h_2 (m)	10	10.2	0.0225	0.31	9.9	0.0562	0.79
	h_3 (m)	5	4.8	0.0302	0.21	5.1	0.0190	0.13
	v_{p1} (m·s^{-1})	350	348.6	0.0055	2.75	352.6	0.0117	5.79
	v_{p2} (m·s^{-1})	700	700.0	0.0002	0.23	685.8	0.0201	0.85
	v_{p3} (m·s^{-1})	450	446.1	0.0097	6.23	443.9	0.0133	4.98
	v_{p4} (m·s^{-1})	1200	1181.9	0.0172	29.34	1236.4	0.0391	6.51
BWO	v_{s1} (m·s^{-1})	220	220.1	0.0019	0.62	221.5	0.0224	6.97
	v_{s2} (m·s^{-1})	420	417.9	0.0048	0.42	443.1	0.0550	12.68
	v_{s3} (m·s^{-1})	260	269.6	0.0369	4.97	253.1	0.0266	0.31
	v_{s4} (m·s^{-1})	710	751.1	0.0579	39.40	720.9	0.0153	6.43
	h_1 (m)	2	2.1	0.0544	0.03	1.9	0.0330	0.09
	h_2 (m)	10	10.1	0.0115	0.16	9.4	0.0559	0.23
	h_3 (m)	5	4.8	0.0240	0.03	4.9	0.0193	0.13
	v_{p1} (m·s^{-1})	350	369.6	0.0562	2.95	340.7	0.0265	0.75
	v_{p2} (m·s^{-1})	700	697.1	0.0042	2.32	690.2	0.0139	8.23
	v_{p3} (m·s^{-1})	450	449.3	0.0175	11.15	454.9	0.0347	22.11
	v_{p4} (m·s^{-1})	1200	1160.8	0.0327	55.57	1145.0	0.0458	36.06
PSO	v_{s1} (m·s^{-1})	220	220.8	0.0075	2.34	217.4	0.0114	3.32
	v_{s2} (m·s^{-1})	420	420.2	0.0088	5.22	418.7	0.0080	4.79
	v_{s3} (m·s^{-1})	260	269.6	0.0372	6.61	269.7	0.0373	12.54
	v_{s4} (m·s^{-1})	710	677.1	0.0464	5.49	745.7	0.0504	44.03
	h_1 (m)	2	1.9	0.0392	0.11	1.9	0.0075	0.003
	h_2 (m)	10	9.5	0.0490	0.44	10.1	0.0810	1.14
	h_3 (m)	5	5.3	0.0600	0.15	4.7	0.0518	0.11
	v_{p1} (m·s^{-1})	350	347.2	0.0327	16.21	348.1	0.0190	9.40
	v_{p2} (m·s^{-1})	700	700.8	0.0040	4.03	689.5	0.0148	7.45
	v_{p3} (m·s^{-1})	450	480.3	0.0673	31.74	449.9	0.0104	6.67
	v_{p4} (m·s^{-1})	1200	1143.9	0.0467	9.39	1230.6	0.0560	95.10

Note: Re = relative error.

length of 46 m. An initial source offset of 8 m was adopted to mitigate near-field effects while preserving an adequate signal-to-noise ratio. The seismic source consisted of a 10 kg hammer impacting a rigid plastic plate, with five repeated impacts at each shot location and vertical stacking applied to enhance data quality. In their original study, *Şenkaya et al. (2020)* performed the inversion of Rayleigh-wave dispersion and refraction data using a gradient-based local optimisation algorithm.

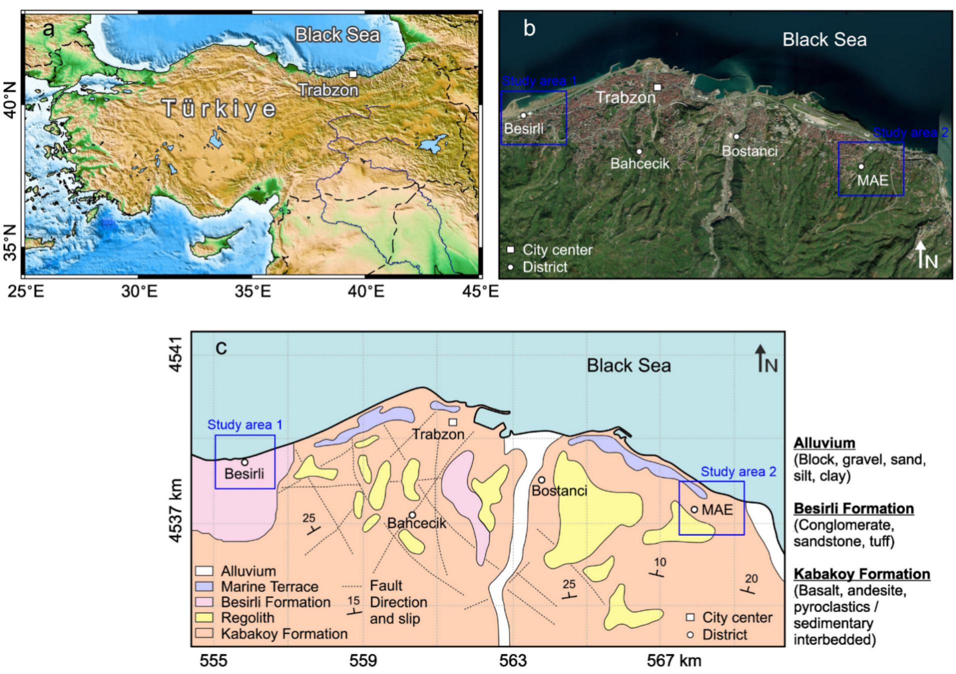

Fig. 7. (a) Location of the two study areas, (b) Topographic map, (c) Geological map of the study areas *Şenkaya et al. (2020)*.

The proximity of the Beşirli site to the coastline suggests the likelihood of seawater infiltration into the subsurface, which can reduce both shear-wave Vs and P-wave Vp velocities, particularly at greater depths. In addition, the presence of weak or water-saturated layers may further complicate the surface-wave dispersion behaviour (*Gao et al., 2016; Mi et al., 2018*), rendering this site particularly suitable for evaluating the effectiveness of joint inversion methodologies.

Using the same inversion settings as those adopted in the synthetic experiments, BWO, EBWO, and Particle Swarm Optimisation (PSO) were applied to both joint and individual inversions of the Beşirli field dataset. The model space, defined based on prior geophysical investigations, is summarised in Table 4. The corresponding inversion results are presented in Figs. 8 and 9.

Table 4. Model space constructed from available geophysical results from *Şenkaya et al. (2020)* regarding the Beşirli site.

Layers	v_s (m/s)	h (m)	v_p (m/s)
1	$50 \sim 400$	$0.5 \sim 5$	$100 \sim 900$
2	$130 \sim 760$	$1 \sim 7$	$200 \sim 1500$
3	$40 \sim 300$	$0.8 \sim 5$	$300 \sim 2200$
4	$100 \sim 600$	$0.6 \sim 4$	$500 \sim 3000$
Half-space	$90 \sim 550$		$400 \sim 2500$

Figure 8 illustrates the data-fitting performance of each algorithm under both inversion schemes. As expected for field data inherently affected by noise and environmental interference, all three algorithms achieved satisfactory fits, with only minor differences in misfit between joint and individual inversions. However, more substantial discrepancies became apparent in the reconstructed subsurface velocity structures.

As shown in Figure 9, the *Vs* and *Vp* models obtained using EBWO exhibit closer agreement with previous regional interpretations by *Şenkaya et al. (2020)* than those derived from BWO and PSO. Among all the evaluated approaches, joint inversion using EBWO yields the most geologically consistent results, thereby underscoring the advantages of integrating complementary geophysical datasets. Across all algorithms, joint inversion consistently outperforms individual inversion, particularly at greater depths, where the sensitivity of individual datasets is typically reduced.

The inversion results further indicate that the shallow subsurface in the Beşirli area can be subdivided into five distinct layers (Fig. 9). A pronounced reduction in shear-wave velocity below approximately 6 m depth is especially evident, which is consistent with the anticipated effects of seawater intrusion. Such conditions can degrade the mechanical properties of subsurface materials and reduce seismic velocities in porous or fractured

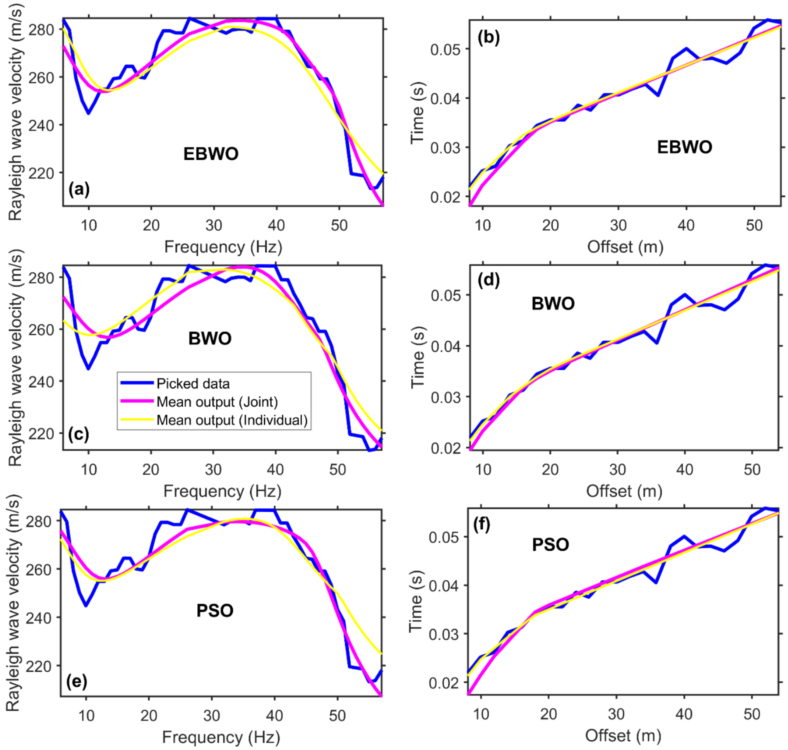

Fig. 8. Joint and independent inversion results using BWO, EBWO, and PSO for fitting Rayleigh wave dispersion curves and refraction data from the Beşirli area. Blue: field data; pink: joint inversion; yellow: independent inversion. Please refer to the text for more details.

formations.

Figure 10 presents the convergence behaviour of the BWO, EBWO, and PSO algorithms during the joint inversion of the Beşirli dataset, with logarithmic scaling applied to the horizontal axis to better resolve the early-stage convergence characteristics. Although the overall convergence trends are broadly similar, the EBWO consistently attains the lowest final misfit, indicating a stronger capacity to approach the global optimum. Tables 5–7 summarise the statistical characteristics of the inversion results, including the mean parameter estimates and standard deviations across multiple independent runs. The EBWO consistently exhibits smaller standard deviations compared with the BWO and PSO algorithms, thereby demonstrating su-

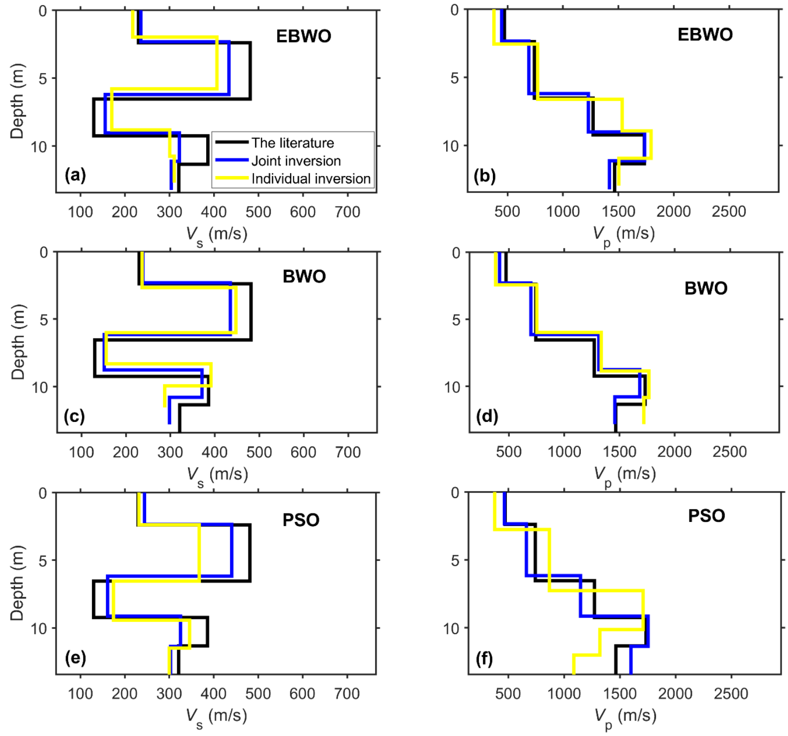

Fig. 9. Joint and independent inversion results of Rayleigh wave and refraction data from the Beşirli area using BWO, EBWO, and PSO. Black: previous inversion results from *Şenkaya et al. (2020)*; blue: joint inversion; yellow: independent inversion. Please refer to the text for more details.

perior stability and robustness under noisy field conditions.

In summary, EBWO provides the most accurate and reliable joint inversion results among the evaluated algorithms. Even when applied to field data subject to significant noise contamination, it successfully recovers subsurface parameters that are in close agreement with independent geophysical interpretations. By achieving an effective balance between data-fitting fidelity and parameter stability, EBWO demonstrates strong potential for practical applications in near-surface geophysical exploration.

The second field dataset, acquired at the MAE site, was likewise digitised from *Şenkaya et al. (2020)* using identical acquisition parameters. The geographic location, topographic characteristics, and geological framework of

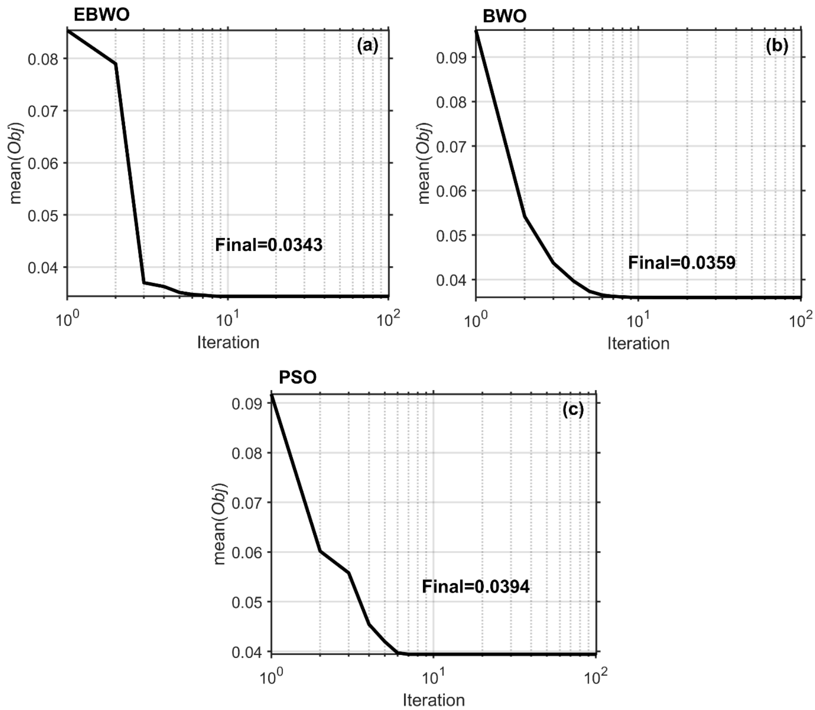

Fig. 10. Iteration process of joint inversion of Rayleigh wave dispersion curves and refraction data from the Beşirli area for saltwater intrusion problem using EBWO (a), BWO (b), and PSO (c).

this area are illustrated in Fig. 7 (study area 2). Following the same workflow adopted for the first field case, BWO, EBWO, and Particle Swarm Optimisation (PSO) were applied to both joint and individual inversions of the MAE dataset. The corresponding model space, summarised in Table 8, was defined based on previously published inversion results from *Şenkaya et al. (2020)*.

The inversion results are presented in Figs. 11 and 12. Figure 11 illustrates the data-fitting performance of each algorithm under both inversion schemes. Consistent with the previous case study, all three methods achieved satisfactory fits to the observed data, with only minor differences in misfit between joint and individual inversions. However, more pronounced discrepancies emerge in the reconstructed subsurface velocity models.

As shown in Figure 12, the shear-wave and P-wave velocity structures

Table 5. Mean results and standard deviations of the joint inversion of Rayleigh wave dispersion and refraction data from the Beşirli area using EBWO.

Layers	v_s (m/s)		h (m)		v_p (m/s)	
	Mean	STD	Mean	STD	Mean	STD
1	235.7	5.72	2.3	0.01	447.3	2.26
2	433.7	10.93	3.8	0.04	690.8	2.91
3	155.5	1.64	2.8	0.05	1228.3	47.19
4	322.2	0.58	2.1	0.03	1736.1	24.88
Half-space	303.8	11.99			1420.0	15.67

Table 6. Mean results and standard deviations of the joint inversion of Rayleigh wave dispersion and refraction data from the Beşirli area using BWO.

Layers	v_s (m/s)		h (m)		v_p (m/s)	
	Mean	STD	Mean	STD	Mean	STD
1	238.2	25.34	2.3	0.10	415.0	7.65
2	434.7	10.85	3.8	0.46	698.4	22.79
3	151.2	9.55	2.6	0.32	1313.3	112.28
4	370.7	11.21	2.0	0.33	1684.1	53.46
Half-space	297.8	24.07			1458.9	27.58

Table 7. Mean results and standard deviations of the joint inversion of Rayleigh wave dispersion and refraction data from the Beşirli area using PSO.

Layers	v_s (m/s)		h (m)		v_p (m/s)	
	Mean	STD	Mean	STD	Mean	STD
1	244.4	5.62	2.3	0.002	463.9	5.19
2	440.4	82.49	3.8	0.33	661.0	0.18
3	160.8	5.73	2.9	0.14	1147.3	99.10
4	324.9	3.78	2.2	0.09	1752.7	114.87
Half-space	302.92	21.43			1600.1	263.24

obtained using EBWO exhibit closer agreement with earlier regional interpretations by *Şenkaya et al. (2020)* than those derived from BWO and PSO. Among all the evaluated approaches, joint inversion using EBWO yields the most geologically plausible results, further highlighting the benefits of integrating complementary geophysical datasets. Across all algorithms, joint inversion consistently outperforms individual inversion, providing an improved delineation of subsurface structures, particularly in zones where single datasets exhibit limited sensitivity.

Table 8. Model space constructed from available geophysical results from *Şenkaya et al. (2020)* regarding the MAE site.

Layers	v_s (m/s)	h (m)	v_p (m/s)
1	$50 \sim 300$	$0.5 \sim 3$	$140 \sim 500$
2	$100 \sim 500$	$1 \sim 7$	$300 \sim 1000$
Half-space	$400 \sim 1600$	∞	$1000 \sim 3200$

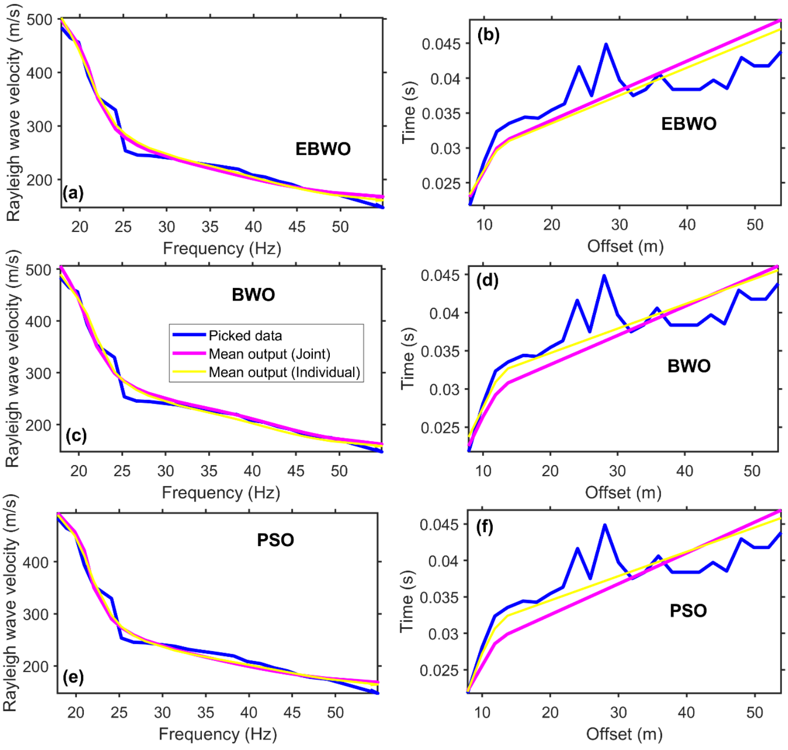

Fig. 11. Joint and independent inversion results obtained using BWO, EBWO, and PSO for Rayleigh wave dispersion curves and refraction data from the MAE site. Blue curves denote the field data; pink curves represent joint inversion results; yellow curves correspond to independent inversion results. Further details are provided in the main text.

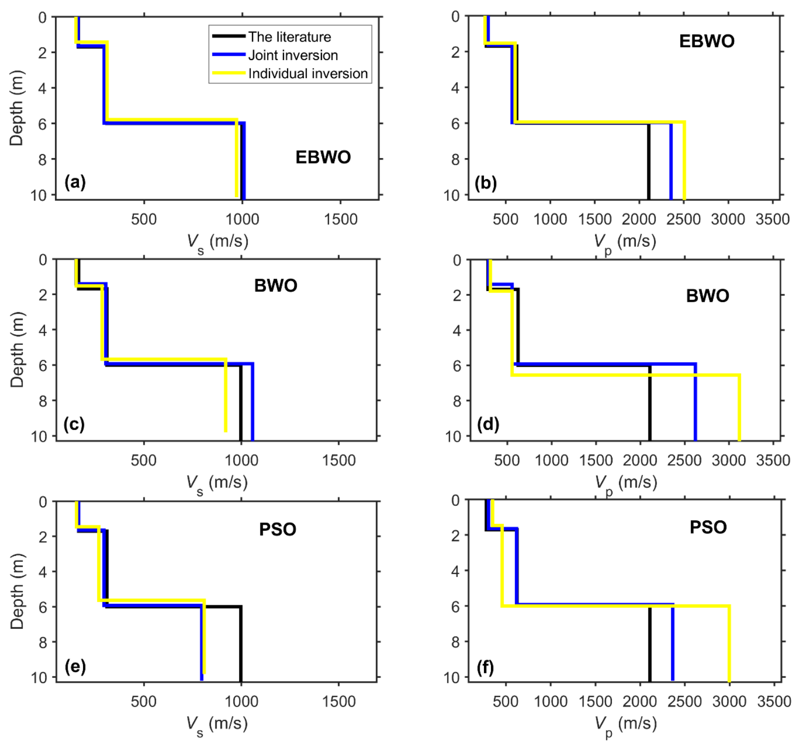

Fig. 12. Joint and independent inversion results of Rayleigh wave and refraction data from the MAE site using BWO, EBWO, and PSO. Black: previous inversion results from *Şenkaya et al. (2020)*; blue: joint inversion; yellow: independent inversion. Please refer to the text for more details.

Notably, the near-surface layer identified from the joint inversion results is interpreted as clay containing sand and/or gravel, which is in good agreement with borehole observations reported for the study area. This consistency provides additional validation of the reliability of the inversion framework.

Figure 13 presents the convergence behaviour of the BWO, EBWO, and PSO methods during the joint inversion of the MAE dataset, with logarithmic scaling applied to the horizontal axis to enhance the visualisation of early-stage convergence. Although the overall convergence patterns are broadly similar, the EBWO consistently achieves the lowest final misfit, indicating a stronger ability to approach the global optimum. Tables 9–11

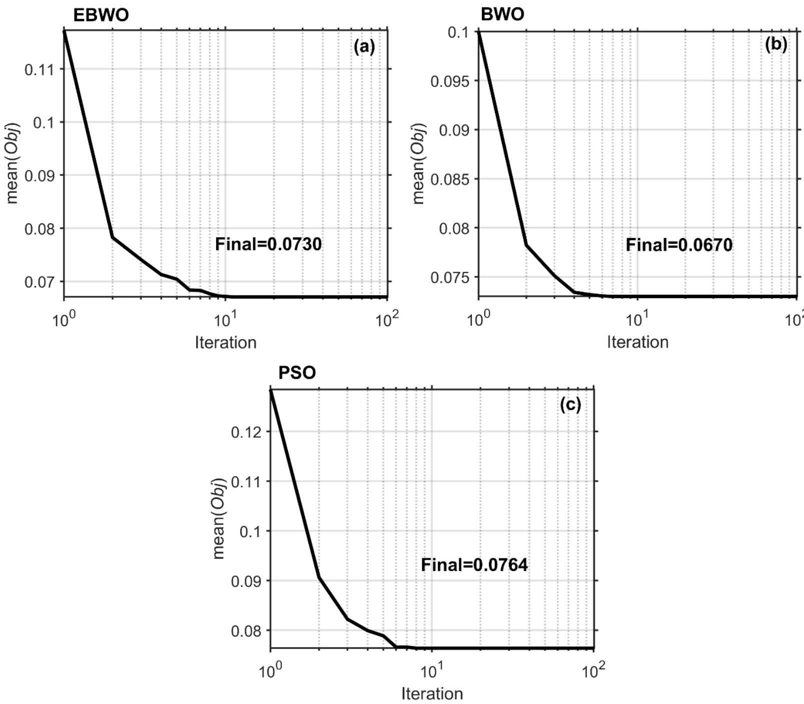

Fig. 13. Iteration process of joint inversion of Rayleigh wave dispersion curves and refraction data from the MAE site for saltwater intrusion problem using EBWO (a), BWO (b), and PSO (c).

summarise the statistical characteristics of the inversion results, including the mean parameter estimates and standard deviations across multiple independent runs. The EBWO consistently yields smaller standard deviations than the BWO and PSO methods, thereby demonstrating superior stability and robustness under realistic field conditions.

Furthermore, the recovered velocity structures indicate that the primary competent rock unit occurs at depths greater than approximately 6 m, which is consistent with the range reported in previous investigations (*Babacan, 2013; Şenkaya et al., 2020*).

Overall, these findings further substantiate the reliability, accuracy, and practical applicability of EBWO for joint inversion in complex near-surface environments, reinforcing its potential as a robust tool for integrated geophysical interpretation.

Table 9. Mean results and standard deviations of the joint inversion of Rayleigh wave dispersion and refraction data from the MAE site using EBWO.

Layers	v_s (m/s)		h (m)		v_p (m/s)	
	Mean	STD	Mean	STD	Mean	STD
1	163.9	0.11	1.6	0.09	302.4	5.31
2	297.1	10.08	4.3	0.11	572.5	28.30
Half-space	1008.0	41.22			2356.2	63.73

Table 10. Mean results and standard deviations of the joint inversion of Rayleigh wave dispersion and refraction data from the MAE site using BWO.

Layers	v_s (m/s)		h (m)		v_p (m/s)	
	Mean	STD	Mean	STD	Mean	STD
1	150.6	6.09	1.4	0.03	288.9	3.61
2	304.1	9.02	4.5	0.49	557.0	51.40
Half-space	1057.4	115.91			2619.1	19.45

Table 11. Mean results and standard deviations of the joint inversion of Rayleigh wave dispersion and refraction data from the MAE site using PSO.

Layers	v_s (m/s)		h (m)		v_p (m/s)	
	Mean	STD	Mean	STD	Mean	STD
1	164.6	4.12	1.64	0.22	306.1	6.88
2	294.5	11.00	4.28	0.08	616.7	18.55
Half-space	796.6	108.77			2363.7	95.53

6. Discussion

One of the persistent challenges in the inversion of surface-wave data for resolving near-surface shear-wave velocity (Vs) structures lies in the parameterization and discretization of subsurface layering. The choice of layer number exerts first-order control on model resolution, stability, and inversion accuracy. A range of strategies has been proposed to address this issue. For instance, *Killingbeck et al. (2018)* employed a transdimensional Markov chain Monte Carlo (MCMC) framework to explore models with variable layer configurations. Similarly, *Wang et al. (2024)* developed a global optimisation scheme capable of simultaneously inverting both layer parameters and layer count. More recently, *Ai et al. (2025b; 2026)* introduced computationally efficient transdimensional inversion approaches that enable the adaptive estimation of the layer number without substantially enlarging the model space.

Despite these advances, treating the number of layers as an unknown parameter inevitably increases model complexity by expanding the dimensionality of the search space. This increased dimensionality poses significant challenges for stochastic optimisation algorithms, particularly in maintaining an effective balance between global exploration and local exploitation. Moreover, many existing inversion schemes adopt broad parameter bounds for the layer number, shear-wave velocity, and P-wave velocity without incorporating prior constraints on physically realistic property contrasts. Such wide search intervals expand the feasible model space and reduce computational efficiency.

In the present study, this issue is not explicitly addressed, as prior geophysical investigations provide sufficiently robust constraints on the stratigraphic framework of the study area. Nevertheless, the development of efficient and physically informed strategies for estimating the layer number remains an important area for future research. One promising alternative is the adoption of finely discretised models with uniformly spaced layers, thereby avoiding the need to treat the layer number as an explicit inversion parameter.

Another well-recognized challenge in surface-wave inversion is the mode-kissing phenomenon, in which overlapping dispersion modes hinder reliable mode identification and phase-velocity picking. Although this issue falls beyond the scope of the present study, it merits further attention. Several approaches have been proposed to mitigate its impact. High-resolution transformation techniques, such as the vector wavenumber transformation method (*Yang et al., 2019*), can enhance dispersion image clarity and improve mode separation. In addition, deep learning–based automatic dispersion picking methods (*Song et al., 2022*) have been shown to reduce the risk of mode misidentification. *Zhang et al. (2022)* further proposed a sequential joint inversion framework incorporating multiple modes to improve mode discrimination. Alternative strategies include workflows that bypass manual mode identification altogether (*Yan et al., 2022*), as well as methods that apply Particle Swarm Optimisation (PSO) directly to the frequency–velocity spectrum (FVS), thereby eliminating the need for explicit dispersion curve extraction (*Le et al., 2024*). The implementation of joint inversion of multi-mode dispersion and refraction data warrants further investigation and may improve the reliability of inversion results.

7. Conclusions

This study applies an Enhanced Beluga Whale Optimisation (EBWO) algorithm to the joint inversion of Rayleigh wave dispersion curves and seismic refraction data. The methodology is validated through benchmark tests on multimodal functions, synthetic experiments under both noise-free and noisy conditions, and field applications in the Beşirli and MAE regions (Türkiye), characterised by complex geological settings. The main findings are summarised as follows:

(i) Robust nonlinear optimisation framework

EBWO demonstrates strong performance as a nonlinear optimisation approach, particularly for high-dimensional problems with limited prior constraints. Compared with individual inversions, the joint inversion strategy significantly improves the estimation of the layer thickness, shear-wave velocity, and P-wave velocity, enhancing both model accuracy and stability.

(ii) Improved exploration and convergence

Algorithmic enhancements, including Tent chaotic mapping and opposition-based learning, improve global exploration in the early stages and accelerate convergence in later iterations. These benefits are most evident with moderate-to-large population sizes, sufficient iteration numbers, and well-sampled datasets. Reliable convergence requires appropriate parameter selection, with larger populations and iterations recommended when necessary.

(iii) Strong performance on field data

Field applications have shown that EBWO produces results more consistent with independent geophysical interpretations than the original

BWO and Particle Swarm Optimisation (PSO), confirming its robustness under complex geological conditions.

(iv) Broad applicability

Beyond this study, EBWO is applicable to a wide range of geophysical inversion problems, including self-potential, gravity, magnetic, and seismic source inversion.

Overall, EBWO provides an efficient, stable, and flexible optimisation framework for near-surface geophysical investigations and holds significant potential for broader multi-parameter inversion applications.

Author contributions. All authors contributed to the conceptualisation of this research and the computer implementation of the methods. All authors have read and agreed to the published version of the manuscript.

Conflict of interest. The authors declare no conflicts of interest relevant to this study.

Acknowledgements. The field datasets from Türkiye were digitised from the study of *Şenkaya et al. (2020)*, which is greatly acknowledged. The code for all benchmark functions in the paper can be downloaded from `http://www.sfu.ca/~ssurjano`. We thank Dr. Hanbing Ai for carefully reviewing this paper.

Funding. The author(s) declare that financial support was received for the research, authorship, and/or publication of this article. This work was supported by the Jiangxi Province Education Science "14th Five-Year Plan" 2023 Annual Project, Research on Personalized Learning Driven by the Synergy of Knowledge Graphs and Educational Big Data (No. 23YB296), and the Major Science and Technology Innovation Team Development Program of Nanchang Normal University (No. NCNUCXTD002).

References

Ai H., Abdelrahman K., Eldosouky A. M., 2026: Full-parametric, transdimensional, and joint inversion of surface wave dispersion and earthquake-based HVSR by MBMO for obtaining reliable subsurface structures. Sci. Rep., **16**, 4312, doi: 10.1038/s41598-025-16557-6.

Ai H., Ekinci Y. L., Balkaya Ç., Alvandi A., Ekinci R., Roy A., Su K., Pham L. T., 2024a: Modified Barnacles mating optimizing algorithm for the inversion of self-potential anomalies due to ore deposits. Nat. Resour. Res., **33**, 3, 1073–1102, doi: 10.1007/s11053-024-10331-7.

Ai H., Essa K. S., Ekinci Y. L., Balkaya Ç., Géraud Y., 2024b: Hunger Games Search optimization for the inversion of gravity anomalies of active mud diapir from SW

Taiwan using inclined anticlinal source approximation. J. Appl. Geophys., **227**, 105443, doi: 10.1016/j.jappgeo.2024.105443.

Ai H., Song X., Zhang X., Ekinci Y. L., Balkaya Ç., Shekar B., Le Z., Yan Y., 2025a: Full-parametric and joint inversion of multimode surface wave data for identifying glacial ice thickness and freezing extent in subglacial sediments via the hunger games search algorithm. Geophysics, **90**, 1, KS1–KS14, doi: 10.1190/geo2023-0756.1.

Ai H., Song X., Zhang X., Ekinci Y. L., Balkaya Ç., Roy A., Li J., Ning L., Le Z., Yan Y., 2025b: Transdimensional joint inversion of surface wave, refraction, and resistivity data using Modified Barnacles Mating Optimizer for near-surface investigations. J. Appl. Geophys., **241**, 105863, doi: 10.1016/j.jappgeo.2025.105863.

Babacan A. E., 2013: The determination of engineering properties of volcanic rocks of Kabaköy Formation (Trabzon) with seismic tomography method. PhD Thesis, Karadeniz Technical University, Trabzon (in Turkish).

Balkaya Ç., Ekinci Y. L., Ai H., Biswas A., Göktürkler G., 2024: Fault structure reconstruction from magnetic anomalies using an improved backtracking search optimization algorithm. Earth Space Sci., **11**, 5, e2023EA003082, doi: 10.1029/2023EA003082.

Cao J., Liu J., Yin H., Cai Z., Yang Q., Yang H., Zhu Y., 2025: Can the compressed sensing theory be utilized in active source surface wave exploration? A primary result. J. Geophys. Eng., **22**, 1, 149-164, doi: 10.1093/jge/gxae125.

Ekinci Y. L., Ai H., Balkaya Ç., Roy A., 2025a: 2.75-D Global joint inversion of gravity and magnetic anomalies with appraisal of model reconstruction uncertainty. J. Appl. Geophys., **245**, 106036, doi: 10.1016/j.jappgeo.2025.106036.

Ekinci Y. L., Balkaya Ç., Ai H., Roy A., Özyalin Ş., 2025b: Investigation of Kula Volcanic Field (Türkiye) Through the Inversion of Aeromagnetic Anomalies Using Success-History-Based Adaptive Differential Evolution with Exponential Population Reduction Strategy. Pure Appl. Geophys., **182**, 3, 1333–1361, doi: 10.1007/s00024-024-03569-y.

Ekinci Y. L., Balkaya Ç., Göktürkler G., Ai H., 2023: 3-D gravity inversion for the basement relief reconstruction through modified success-history-based adaptive differential evolution. Geophys. J. Int., **235**, 1, 377–400, doi: 10.1093/gji/ggad222.

Fan Y.-H., Liu J.-Q., Xiao B.-X., 2002: Fast vector-transfer algorithm for computation of Rayleigh wave dispersion curves. J. Hunan Univ. Nat. Sci., **29**, 5, 25–30, doi: 10.3321/j.issn:1000-2472.2002.05.006 (in Chinese).

Fu Y., Ai H., Yao Z., Li H., Tian X., Zhang X., 2023a: Inversion of multi-mode Rayleigh wave dispersion curves based on lightning attachment procedure optimization. Oil Geophys. Prospect., **58**, 830–838, doi: 10.13810/j.cnki.issn.1000-7210.2023.04.008 (in Chinese).

Fu Y., Ai H., Yao Z., Mei Z., Su K., 2023b: Inversion of the Rayleigh wave dispersion curves based on the sine-cosine algorithm. Geophys. Geochem. Explor., **47**, 6, 1467–1478, doi: 10.11720/wtyht.2023.1239 (in Chinese).

Gao L., Xia J., Pan Y., Xu Y., 2016: Reason and condition for mode kissing in MASW method. Pure Appl. Geophys., **173**, 5, 1627–1638, doi: 10.1007/s00024-015-1208-5.

Gao X., Yu J., Li X., Hu T., He C., Yue Y., 2021: Rayleigh wave dispersion curve inversion based on adaptive weight dragonfly algorithm. Oil Geophys. Prospect., **56**, 4, 745–757, doi: 10.13810/j.cnki.issn.1000-7210.2021.04.008 (in Chinese).

Ivanov J., Miller R. D., Xia J., Steeples D., Park C. B., 2006: Joint analysis of refractions with surface waves: An inverse solution to the refraction-traveltime problem. Geophysics, **71**, 6, R131–R138, doi: 10.1190/1.2360226.

Killingbeck S. F., Livermore P. W., Booth A. D., West L. J., 2018: Multimodal layered transdimensional inversion of seismic dispersion curves with depth constraints. Geochem. Geophys. Geosyst., **19**, 12, 4957–4971, doi: 10.1029/2018GC008000.

Le Z., Song X., Zhang X., Shen C., Ai H., Yuan S., Fu D., 2024: Particle swarm optimization for Rayleigh wave frequency-velocity spectrum inversion. J. Appl. Geophys., **222**, 105311, doi: 10.1016/j.jappgeo.2024.105311.

Lo T.-w., Inderwiesen P. L., 1994: Fundamentals of Seismic Tomography. Society of Exploration Geophysicists, Tulsa, OK,y 188 p.

Meyer C. D., 2023: Matrix Analysis and Applied Linear Algebra. 2nd edn, Society for Industrial and Applied Mathematics, Philadelphia, PA, 1005 p.

Mi B., Xia J., Shen C., Wang L., 2018: Dispersion energy analysis of Rayleigh and Love waves in the presence of low-velocity layers in near-surface seismic surveys. Surv. Geophys., **39**, 2, 271–288, doi: 10.1007/s10712-017-9440-4.

Michalewicz Z., 1996: Genetic Algorithms + Data Structures = Evolution Programs. Springer Science & Business Media, 387 p.

Ning L., Dai T., Ai H., Zhang H., Zheng L., 2026: Enhancing karst cave detection in Hangzhou using stationary-phase traffic noise imaging with seismic interferometry. Geophysics, **91**, 1, B35–B52, doi: 10.1190/geo2025-0080.

Ning L., Dai T., Huang G., Liu L., Ai H., Xi C., 2025: Near-surface geothermal reservoir exploration by multichannel analysis of passive surface waves using urban traffic noise in Shanxi. J. Appl. Geophys., **244**, 106032, doi: 10.1016/j.jappgeo.2025.106032.

Pan D., Gao J., Zhang H., 2025: Improving passive seismic surface-wave dispersion measurement deteriorated by strong fixed-frequency interference in the industry environment. J. Geophys. Eng., **22**, 4, 986–1002, doi: 10.1093/jge/gxaf053.

Park C. B., Miller R. D., Xia J., 1999: Multichannel analysis of surface waves. Geophysics, **64**, 3, 800–808, doi: 10.1190/1.1444590.

Peng L., Feng W., Xie H., Li F., Yang Y., Cao J., Ren C., 2024: An improved butterfly optimization algorithm in the inversion of Rayleigh wave dispersion curve. Geophys. Geochem. Explor., **48**, 3, 705–720, doi: 10.11720/wtyht.2024.1116 (in Chinese with English abstract).

Piatti C., Socco L. V., Boiero D., Foti S., 2013: Constrained 1D joint inversion of seismic surface waves and P-refraction traveltimes. Geophys. Prospect., **61**, s1, 77–93, doi: 10.1111/j.1365-2478.2012.01071.x.

Poormirzaee R., 2018: MOPSO: a new computing algorithm for joint inversion of Rayleigh wave dispersion curve and refraction traveltimes. Explor. Geophys., **49**, 2, 163–175, doi: 10.1071/EG16044.

Poormirzaee R., 2022: Seismic refraction data inversion via jellyfish search algorithm for bedrock characterization in dam sites. SN Appl. Sci., **4**, 10, 288, doi: 10.1007/s42452-022-05171-0.

Şenkaya M., Karsli H., Socco L. V., Foti S., 2020: Obtaining reliable S-wave velocity depth profile by joint inversion of geophysical data: the combination of active surface-wave, seismic refraction and electric sounding data. Near Surf. Geophys., **18**, 6, 659–682, doi: 10.1002/nsg.12126.

Shan L., Qiang H., Li J., Wang Z., 2005: Chaotic optimization algorithm based on Tent map. Control Decis., **20**, 2, 179–182.

Song W., Feng X., Zhang G., Gao L., Yan B., Chen X., 2022: Domain adaptation in automatic picking of phase velocity dispersions based on deep learning. J. Geophys. Res. Solid Earth, **127**, 6, e2021JB023389, doi: 10.1029/2021JB023389.

Song X., Tang L., Lv X., Fang H., Gu H., 2012: Application of particle swarm optimization to interpret Rayleigh wave dispersion curves. J. Appl. Geophys., **84**, 1–13, doi: 10.1016/j.jappgeo.2012.05.011.

Soske J. L., 1959: The blind zone problem in engineering geophysics. Geophysics, **24**, 2, 359–365, doi: 10.1190/1.1438597.

Su K., Ai H., Alvandi A., Lyu C., Wei X., Qin Z., Tu Y., Yan Y., Nie T., 2024: Hunger Games Search for the elucidation of gravity anomalies with application to geothermal energy investigations and volcanic activity studies. Open Geosci., **16**, 1, 20220641, doi: 10.1515/geo-2022-0641.

Sun C.-Y., Wang Y.-Y., Wu D.-S., Qin X.-J., 2017: Nonlinear Rayleigh wave inversion based on the shuffled frog-leaping algorithm. Appl. Geophys., **14**, 4, 551–558, doi: 10.1007/s11770-017-0641-x.

Tang S., Wu Y., 2024: Application of modified wild horse optimizer for inversion of base-mode Rayleigh wave dispersion curve. Prog. Geophys., **39**, 4, 1698–1710, doi: 10.6038/pg2024HH0304 (in Chinese).

Wang X., Feng X., Liu Q., Bai H., Dong X., Wang T., 2024: Adaptive trans-dimensional inversion of multimode dispersion curve based on slime mold algorithm. Acta Geophys., **72**, 1, 233–245, doi: 10.1007/s11600-023-01086-5.

Wang Z., Sun C., Wu D., 2023: Near-surface site characterization based on joint iterative analysis of first-arrival and surface-wave data. Surv. Geophys., **44**, 2, 357–386, doi: 10.1007/s10712-022-09747-8.

Wu F., Wei X., He K., Li G., Xu X., 2025: Inversion of Rayleigh wave dispersion curve based on beluga whale optimization algorithm. Contrib. Geophys. Geod., **55**, 4, 393–418, doi: 10.31577/congeo.2025.55.4.1.

Xia J., Miller R. D., Park C. B., 1999: Estimation of near-surface shear-wave velocity by inversion of Rayleigh waves. Geophysics, **64**, 3, 691–700, doi: 10.1190/1.1444578.

Xia J., Miller R. D., Park C. B., Tian G., 2003: Inversion of high frequency surface waves with fundamental and higher modes. J. Appl. Geophys., **52**, 1, 45–57, doi: 10.1016/S0926-9851(02)00239-2.

Yamanaka H., Ishida H., 1996: Application of genetic algorithms to an inversion of surface-wave dispersion data. Bull. Seismol. Soc. Am., **86**, 2, 436–444, doi: 10.1785/BSSA0860020436.

Yan Y., Chen X., Huai N., Guan J., 2022: Modern inversion workflow of the multimodal surface wave dispersion curves: staging strategy and Pattern search with embedded Kuhn–Munkres algorithm. Geophys. J. Int., **231**, 1, 47–71, doi: 10.1093/gji/ggac178.

Yang B., Xiong Z., Zhang D., Yang Z., 2019: Rayleigh surface-wave dispersion curve inversion based on adaptive chaos genetic particle swarm optimization algorithm. Oil Geophys. Prospect., **54**, 6, 1217–1227, doi: 10.13810/j.cnki.issn.1000-7210.2019.06.005 (in Chinese with English abstract).

Yang X.-H., Han P., Yang Z., Chen X., 2023: Two-stage broad learning inversion framework for shear-wave velocity estimation. Geophysics, **88**, 1, WA219–WA237, doi: 10.1190/geo2022-0060.1.

Yang X.-H., Han P., Yang Z., Miao M., Sun Y.-C., Chen X., 2022: Broad learning framework for search space design in Rayleigh wave inversion. IEEE Trans. Geosci. Remote Sens., **60**, 4512617, doi: 10.1109/TGRS.2022.3208616.

Yang X.-H., Zhou Y., Han P., Feng X., Chen X., 2024: Near-surface Rayleigh wave dispersion curve inversion algorithms: a comprehensive comparison. Surv. Geophys., **45**, 3, 773–818, doi: 10.1007/s10712-024-09826-y.

Yang Z., Chen X., Pan L., Wang J., Xu J., Zhang D., 2019: Multi-channel analysis of Rayleigh waves based on Vector Wavenumber Tansformation Method (VWTM). In: Geophysical Research Abstracts, Vol. 21, EGU2019-2595, EGU General Assembly 2019.

Yu D., Song X., Zhang X., Zhao S., Cai W., 2019: Rayleigh wave dispersion inversion based on grasshopper optimization algorithm. Oil Geophys. Prospect., **54**, 2, 288–301, doi: 10.13810/j.cnki.issn.1000-7210.2019.02.007 (in Chinese).

Zhang D., Yang B., Yang Z., Zhang M., Xiong Z., Zhu D., Zhang X., 2022: Multimodal inversion of Rayleigh wave dispersion curves based on a generalized misfit function. J. Appl. Geophys., **207**, 104849, doi: 10.1016/j.jappgeo.2022.104849.

Zhang N., Zhao Z., Bao X., Qian J., Wu B., 2020: Gravitational search algorithm based on improved Tent chaos. Control Decis., **35**, 4, 893–900, doi: 10.13195/j.kzyjc.2018.0795 (in Chinese with English abstract).

Zhong C., Li G., Meng Z., 2022: Beluga whale optimization: A novel nature-inspired metaheuristic algorithm. Knowl. Based Syst., **251**, 109215, doi: 10.1016/j.knosys.2022.109215.